JOURNAL OF GEOPHYSICAL RESEARCH, VOL. 107, NO. D10, 4104, 10.1029/2001JD000426, 2002

Regional radiative forcing by line-shaped contrails derived from satellite data

R. Meyer, H. Mannstein, R. Meerkötter, U. Schumann, and P. Wendling
Institut für Physik der Atmosphäre, Deutsches Zentrum für Luft- und Raumfahrt, DLR Oberpfaffenhofen, Germany

Received 22 January 2001; revised 25 July 2001; accepted 26 July 2001; published 31 May 2002.

[1] The influence of contrails on the radiation budget depends mainly on their coverage and optical depth. This study derives these parameters from data of the advanced very high resolution radiometer sensor onboard the NOAA 14 satellite for a region over western Europe within 40°–56°N and 10°W–23°E during 2 years starting March 1995. The data are classified by an operational contrail detection algorithm with a new evaluation of the detection efficiency. From the classification results, daytime and nighttime coverage by line-shaped contrails over western Europe are derived. The daytime contrail coverage for the analyzed region is 0.7% in the annual mean, 1.0% during winter, and 0.4% during summer. The daytime contrail cover is 3 times higher than the night-time contrail cover. An effective optical depth of the observed contrails is derived from the radiation contrasts in the 11 μm channel for contrails and adjacent pixels. The optical depth in the visible spectral range is computed from these results assuming a previously measured size spectrum of ice crystals. The mean visible optical depth is found to be about 0.1, much smaller than that derived from previous case studies. The average radiative forcing at the top of the atmosphere is computed for the derived contrail cloud cover and optical depth. Here contrails mostly cause positive radiative forcing (heating). Larger heating effects during night and summer get partly compensated through more contrail cover during day and winter. The radiative forcing by contrails in the examined region is ~0.03 W m^{-2}, which is much smaller than was estimated earlier. *INDEX TERMS:* 1640 Global Change: Remote sensing; 3309 Meteorology and Atmospheric Dynamics: Climatology (1620); 3359 Meteorology and Atmospheric Dynamics: Radiative processes; 9335 Information Related to Geographic Region: Europe; *KEYWORDS:* air traffic, NOAA-AVHRR, contrail coverage, contrail emissivity, contrail optical depth, global warming

1. Introduction

[2] Condensation trails (contrails) are visible traces of aircraft cruising in cold air masses. Contrails persist sometimes for an order of an hour or more and may grow in cover in humid air masses. For some time, contrails keep a linear shape. After a few minutes such line-shaped contrails often are thick and wide enough to become visible in satellite data. Contrails are frequently observed in regions with dense air traffic such as over Europe and North America. Similar to thin cirrus clouds, contrails are composed of ice particles. An increase in cirrus clouds can contribute to global warming [*Liou*, 1986]. The warming can be measured to first approximation by the top of atmosphere instantaneous net radiative forcing [*International Panel on Climate Change* (*IPCC*), 1996].

[3] Aviation is a strongly expanding business, and its influence on climate is still poorly known. Therefore the *IPCC* [1999] recently reported a special study on "Aviation and the Global Atmosphere". The Forecasting and Economic Support Group of the International Civil Aviation Organization (ICAO) provided a possible scenario Fa1 for the future in which air traffic is assumed to increase on average by 3.1% yr^{-1} terms of revenue passenger kilometers, which is equivalent to a factor of 6 over the period 1990–2050 [*Henderson and Wickrama*, 1999]. With more efficient aircraft, improved operation, and optimized routing, aviation fuel usage is expected to triple in the same scenario. Since contrail coverage is strongly related either to traveled airplane distance or fuel consumption, it will rise strongly [*Gierens et al.*, 1999]. This is of concern because contrails may cause more radiative forcing that are caused by the additional carbon dioxides emitted by aviation [*Fortuin et al.*, 1995].

[4] The IPCC assessment of the climate effect of contrails by *Fahey and Schumann* [1999] is based essentially on just two connected studies. The global contrail coverage was first deduced by *Sausen et al.* [1998], and a first estimate of the global mean radiative forcing due to this cover was derived by *Minnis et al.* [1999]. Contrails were computed in these studies to cover about 0.1% of the globe, causing a global mean radiative forcing of 0.02 W m^{-2}. Regional contrail cover values reached up to 3% and radiative forcing peaked at 0.7 W m^{-2} over northeast France. An independent check of these computations is urgently needed.

[5] The distribution of contrails is estimated by *Sausen et al.* [1998] according to the following procedure: First, the potential contrail cover is derived from 10 years of temperature and humidity data reanalyzed consistently by the European Center for Medium-Range Weather Forecast and using the modified Schmidt-Appleman criterion for the threshold temperature of contrail formation [*Schumann*, 1996, 2000; *Schumann et al.*, 2000]. This potential cover then gets multiplied with the air traffic fuel consumption density according to *Gardner et al.* [1997], which applies to the period 1991–1992. Finally, the product is scaled by a factor to match the observed contrail cover reported for parts of western Europe and the eastern North Atlantic by *Bakan et al.* [1994]. As the latter was derived visually from advanced very high resolution radiometer (AVHRR) quicklooks, the results should be checked by a more objective method.

[6] The radiative forcing depends on the cloud height, on the cover, and on the particle-related radiative properties of the

0148-0227/02/2001JD000426$09.00

contrail clouds, in particular the optical depth in the solar range and on the emissivity in the longwave range. Neither is well known so far. Measurements of optical depth have been reported from a few case studies to vary mostly from 0.05 to 0.5 in the visible spectral range [*Kästner et al.*, 1993; *Palikonda et al.*, 1996; *Jäger et al.*, 1998; *Minnis et al.*, 1998; *Spinhirne et al.*, 1998; *Duda et al.*, 2001]. Optical depth values >1 are rare and usually reached only for short contrail lifetimes, for example, for young contrails in the vortex regime [*Sussmann*, 1999]. Another exeption may be contrails in relatively warm and possibly rising air masses as found by *Gayet et al.* [1996], who reported about a contrail reaching a visible optical depth of 2. Yearly and spatial mean values of the optical thickness of contrails have not been studied up to now.

[7] The dependence of the optical depth on wavelength is a function of the particle shape and size distribution within contrails [*Duda et al.*, 2001; *Strauss et al.*, 1997]. Ice particles in young contrails have been observed to be close to spherical but may become nonspherical after some time, in particular at high ambient temperatures [*Meerkötter et al.*, 1999]. For radiative transfer calculations the size distribution is adequately described by the effective diameter D_e of the particles. *Strauss et al.* [1997] find D_e of ~30 μm from replicator measurements. *Schröder et al.* [2000] report size distributions derived from several in situ measurements. Effective diameters thereafter grow with aging from about 3 μm for 2 min old contrails to about 10 μm or more for about 30 min old contrails. The effective diameters derived from satellite retrievals tend to show bigger crystal sizes. *Palikonda et al.* [1996] and *Duda et al.* [2001] derive effective diameters in the range from 25 to 100 μm. *Betancor-Gothe et al.* [1999] observe a growth from 5 μm for ~5 min old contrails to 90 μm for those half an hour old. Thus we notice a wide variability concerning this parameter.

[8] In this study the contrail cover is derived over western Europe, i.e., in a region where, possibly besides North America, air traffic density is largest. Contrails are determined from satellite data using the method that we described earlier by *Mannstein et al.* [1999]. In comparison to our former work we analyzed twice the amount of data and revised the postprocessing scheme, which both enhance accuracy of the achieved results. We also discuss possible false classification of observed structures as contrails ("false alarm rate"). The false alarm rate of the algorithm will be analyzed in detail, and an estimate on the overall detection efficiency will be given. The improved correction scheme considers regional differences of the false alarm rate and detection efficiency. It further takes into account that the algorithm detects contrails during night more efficiently than during day. This postprocessing scheme leads to nightly and daily contrail coverage maps for all seasons. The results for the contrail cover will be compared with the previous results of *Bakan et al.* [1994]. Besides contrail cover the main purpose of the present paper is to derive a first estimate of the mean optical depth and the radiative forcing of contrails from satellite data over western Europe. The average optical depth of the detected contrails is derived from the brightness temperature contrast between contrail and neighboring pixels. The results for the contrail optical depth will be compared to previous case studies and model assumptions. Weighting the seasonal averages of contrail coverage with radiative transfer calculations, we finally calculate the contrail radiative forcing over western Europe. These results will be compared with those derived by *Minnis et al.* [1999] for the same region. This comparison provides a first independent check of the validity of the global estimates used for the IPCC report.

[9] The contrail detection scheme detects line-shaped contrails only. Therefore the results of our study are limited to this type of relatively young contrail. Thus we cannot contribute to the open question of how otherwise air traffic influences cirrus cloud cover and its microphysical properties [*Minnis et al.*, 1998; *Boucher*, 1999; *Schumann*, 2001].

2. Contrail Coverage

[10] The cover by line-shaped contrails is derived over western Europe, within 40°–56°N and 10°W to 23°E. The satellite data are measured with the AVHRR sensor onboard the NOAA 14 satellite. The data were received at Deutsches Zentrum für Luft- und Raumfahrt (DLR) Oberpfaffenhofen, Germany, during the 2 year period from March 1995 to February 1997.

2.1. Detecting Contrails in AVHRR Data

[11] The contrail detection scheme used for this study is basically a pattern recognition algorithm [*Mannstein et al.*, 1999]. Inputs to the algorithm are the brightness temperatures T_{11} and T_{12} derived from AVHRR channels 4 and 5 at 11 and 12 μm wavelengths. The algorithm operates on T_{12} and the brightness temperature difference $\mathrm{TD} = T_{11} - T_{12}$. To avoid misdetections, both images of T_{12} and TD are normalized by the 5 × 5 pixel local standard deviation SDT_{12} and SDTD, respectively. The mean of both normalized images is screened for contrails by line shaped filters with a kernel size of 19 × 19 pixels. Finally, the candidates for contrail pixels are selected by additional parameters that check radiometric and geometric features typical for contrails through fuzzy logic–based decisions.

[12] In principle, this algorithm is able to detect contrails not only above land and water surfaces but also above underlying clouds. From visual inspections of the results we know that many contrails are detected, especially over stratiform cloud fields.

[13] As noted by *Mannstein et al.* [2000], the performance of the algorithm strongly depends on the specific AVHRR instrument onboard the different NOAA polar orbiters. Small differences in the spectral sensitivity of the channels 4 and 5 or varying misalignments of these channels might be the reason for this sensor dependence. To reach consistent results, we strictly use data from only one sensor. We choose the AVHRR instrument onboard NOAA 14 because for this instrument we found the least misdetections. The sensitivity of the algorithm can be controlled by several free parameters, which is described in detail by *Mannstein et al.* [1999]. To achieve a constant detection rate, we fixed all free parameters to the values mentioned there.

[14] In section 2.2 the characteristics of the contrail classification scheme will be investigated in terms of false alarm rate and detection efficiency. The false alarm rate (FAR) is defined here as the ratio of the amount of falsely contrail-classified pixels to the full amount of pixels analyzed. The detection efficiency (DEF) is the ratio of the amount of correctly classified contrail pixels to the full amount of true contrail pixels. In an ideal algorithm, FAR approaches 0 and DEF reaches 1. These limits are difficult to reach even for much easier classification tasks in remote sensing. If, however, we are able to obtain reliable estimates for both parameters, the results on contrail coverage may be corrected in a statistical sense. This is the aim of the study.

2.2. False Alarms

[15] Contrails are usually thin semitransparent ice clouds that are hard to distinguish from background. Therefore a contrail detection algorithm must be a sensitive tool that consequently has a high probability of misdetections. In principal, false alarms may occur through real image features that look similar to contrails or through data errors that accidentally can produce contrail-like structures.

2.2.1. Artifacts through data errors. [16] Along-track line errors are known from pushbroom remote sensing instruments and can easily be confused with contrails. Since the AVHRR uses a spinning mirror to scan across the track (whiskbroom sensor type), the probability for along-track line errors is negligible. More likely are across-track line errors that could result from calibration graduation or errors. Therefore a whole scan line often differs

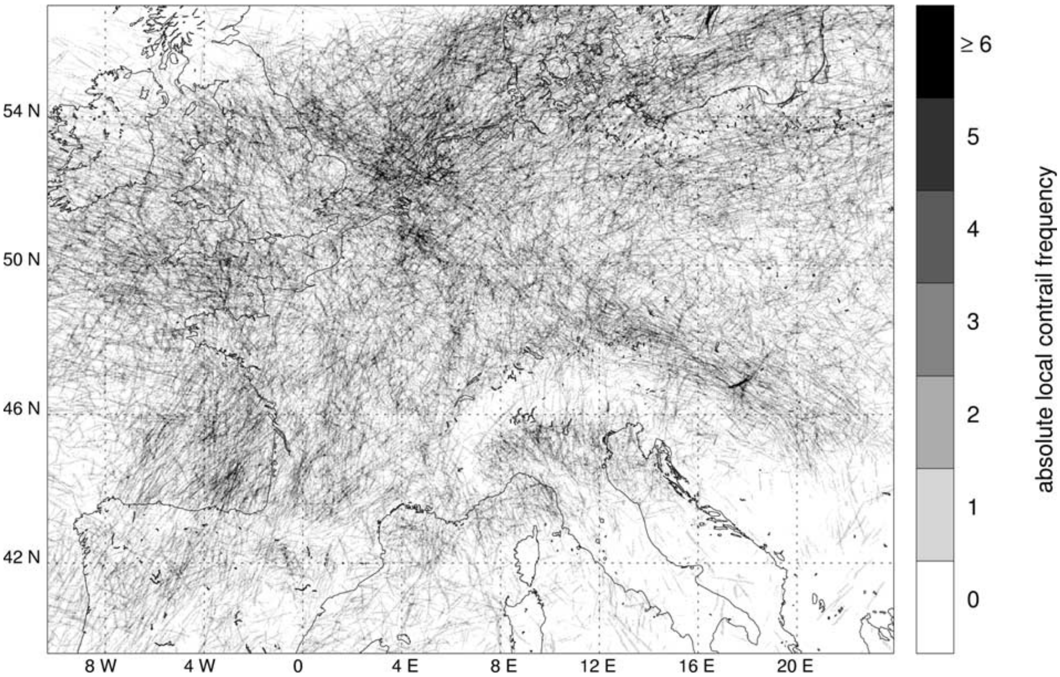

Figure 1. Stacked contrail masks from 702 AVHRR noon passages in the period March 1995 to February 1997.

slightly in its brightness temperatures from the neighboring lines. Occasionally this leads to the radiometric signature of contrails the algorithm is searching for. In this case the geometrical tests will not sort out this artifact, and the whole line could be misclassified. Indeed, some scan lines processed by the original algorithm of *Mannstein et al.* [1999] are found to produce such superlong contrails that can be clearly identified as mistaken. This type of error produced by calibration errors can be successfully avoided by preprocessing the brightness temperature images T_{11} and T_{12}. In case the difference of the local temperature and the median of the temperatures within a 3 × 3 pixel surrounding exceeds a threshold of 10 K the local value will be replaced by the median value. This preprocessing has two advantages: it replaces speckles that make contrail detection harder, and it corrects single bad lines. In case the error influences more than one line it is found by a second routine that searches for outliers of the mean temperature of each line. In this case the ''infected'' lines are not considered in the results. Additionally, the neighboring 19 lines are neglected because this is the size of the biggest filter kernel used in the detection algorithm. In the following we always apply this ''bad line detection'' before the original detection scheme.

[17] The modified contrail detection algorithm is used to analyze each available night and noon scene. All results of contrail classifications for noon are mapped to an equidistant cylindrical grid of ~1 km × 1 km resolution and stacked to the map displayed in Figure 1. As shown in Figure 2 the number of available measurements varies within the analyzed area. The strong lateral dilution is caused by a day to day eastward displacement of the satellite track by ~300 km.

[18] Two types of false alarms still appear in the stacked contrail masks: misdetections of stationary features, usually by line-shaped ground structures, and misdetections of other line-shaped structures within the atmosphere. As the huge number of analyzed satellite data does not allow for interactive editing, statistical methods are applied to correct for errors resulting from image contents.

2.2.2. Stationary artifacts.

[19] In order to find conspicuous outliers (e.g., Figure 3) we assume that the occurrence of contrail pixels in AVHRR data obeys Poisson statistics and obvious exceptions from this must be artifacts. Poisson statistics requires that events are rare and data are sampled randomly. Indeed, contrails are seldom, as even in heavily flown regions, contrail pixels still are a rare phenomena with a probability p_{ct} of the order of 1%. However, is the requirement of random selection fulfilled? First, the precondition for contrail appearance is that there is air traffic in the analyzed region. The air traffic density distribution should be similar at each day to provide equal chances for contrails in each image. As traffic activity patterns are mostly repeated from day to day [*Schmitt and Brunner*, 1997], this requirement is fulfilled but only if similar times of day are analyzed. Furthermore, contrails are only found where atmospheric conditions are suitable for their formation and persistence. Clearly, atmospheric conditions are not independent from one day to the next, and the likelihood to meet favorable contrail conditions varies throughout the year. From these considerations we can derive simple rules that have to be satisfied to obtain a representative average contrail coverage: (1) The sampling should happen at similar times of day; (2) the sampling periods should be much longer than typical periods of weather patterns; and (3) the analyzed data must evenly contain all seasons. These conditions are approximately satisfied in our study so that the selection is sufficiently random and Poisson statistics may be applied.

[20] These statistical characteristics are now used to find outliers in contrail data that might lead to regional errors of contrail coverage. To reach a reliable detection of outliers, we need a huge number of satellite scenes covering the same region. Figure 3 shows a stack of detected contrails from 2 years of noon data. In this image the contrail highscores are suspicious as they exactly match the coastline of Lake Balaton. Such pixels with very high contrail frequencies are classified as artifacts if the local contrail frequency p_{ct} surpasses a certain threshold. This threshold is

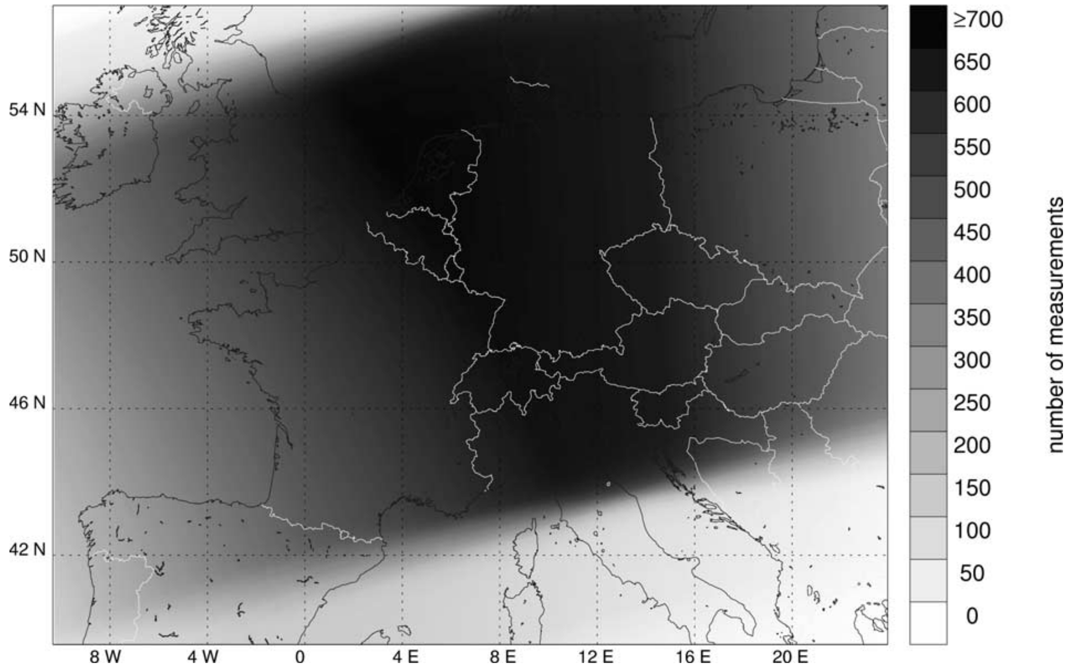

Figure 2. Spatial distribution of the number of measurements for the data shown in Figure 1.

calculated for each point by the Poisson probability for a certain number of contrail pixel detections, where p_{ct} is derived from the average value of the 15 km surrounding. This kernel width was selected because contrails usually appear close to the airways and wind mostly displaces them slightly. If the actual probability to reach a certain contrail frequency value is below 10^{-5}, the pixel will be called a stationary artifact. Then, these 1 km × 1 km boxes are replaced by the average value of the 15 km surrounding. The replacement by the local average prevents underestimation of cover that otherwise would occur if these values would be simply set to

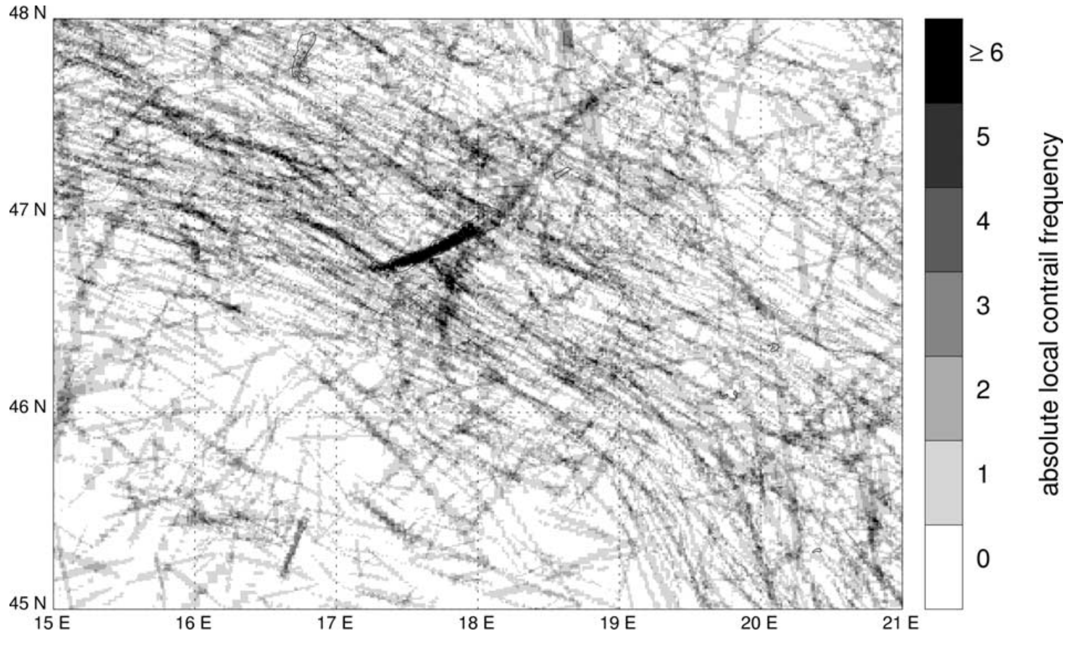

Figure 3. Subset of Figure 1. Lake Balaton a probable stationary artifact is encountered.

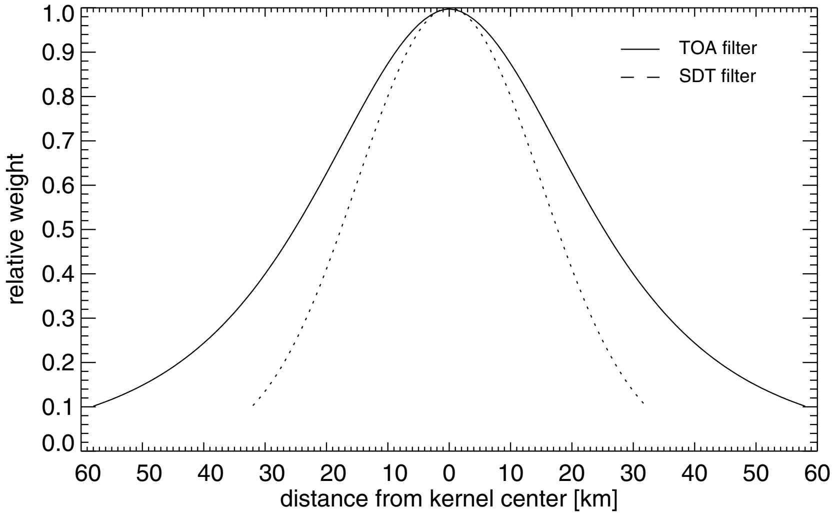

Figure 4. Profiles through the filter kernels used for spatial averaging of frequencies. The wider TOA filter is used to determine the radiative influence of a box that has a certain horizontal distance *d* from the point actually analyzed. The narrower filter is used to derive $\overline{\mathrm{SDT}}_{12}$, which is adapted to the typical size influencing the detection algorithm.

zero. The chosen method avoids having more areas than necessary marked as undefined.

[21] Additionally, Poisson statistics tells us how many satellite scenes are needed to reach significant results. Depending on the expected average local probability p_{ct} for contrail detections,

$$n = -\ln(1 - P)/p_{ct} \tag{1}$$

measurements are needed to reach a certain level of significance *P*. This relationship is very helpful in planning investigations and in deriving the statistical error of the results. For example, in regions with low air traffic density the probability for contrail detections may be only $p_{ct} = 0.002$. Then, according to (1), 1151 measurements are required to reach significant ($P = 90\%$) or even 2303 for highly significant ($P = 99\%$) results. In our data set of 2 years the maximum number of measurements is only about 700. Hence we may not derive significant contrail cover values for many parts of the investigated area on the 1 km × 1 km pixel scale. Therefore spatial averaging is unavoidable to reach meaningful results.

2.2.3. Spatial averaging. [22] For spatial filtering we use a circular filter with the profile shown in Figure 4. This filter is constructed to reflect the influence of various contrail points at horizontal distance *d* from the point under consideration to the radiative forcing felt at top of the atmosphere (TOA). The radiative influence of a contrail pixel of 1 km × 1 km size is assumed to depend on its viewing angle $d\Omega$, which (for a flat Earth approximation) is

$$d\Omega = \left(\arctan\frac{d + 1\mathrm{km}}{\Delta z} - \arctan\frac{d}{\Delta z}\right)^2. \tag{2}$$

For an average contrail altitude of 10 km and an assumed TOA level of $\Delta z = 40$ km above this level, the TOA filter (see Figure 4) implies averaging over about 120 × 120 km^2 of data.

[23] As contrail events are not spatially independent, this spatial averaging alone cannot give us significant results. From a large set of time series we derived the standard deviation of the spatially averaged contrail coverage data $\sigma N'_{ct}$. The standard deviation is found to be proportional to the spatially averaged contrail coverage data N'_{ct} with a slope of 4%/%. This means that the resulting relative standard error of N'_{ct} may be calculated from

$$\frac{\Delta N'_{ct}}{N'_{ct}} = \frac{4}{\sqrt{n}}. \tag{3}$$

Hence at least $n = 64$ measurements are needed to achieve a relative statistical error below 50%. In other words, daily data from more than 2 months are needed to derive meaningful monthly averages of contrail cover values averaged with the given TOA filter.

2.2.4. Nonstationary artifacts. [24] In order to determine the rate of false alarms caused by nonstationary features, for example, cloud streets or streaks of natural cirrus, we utilize AVHRR data from a region almost free of contrails. For this purpose, data from the New Zealand region are chose where climate is similar to Europe and air traffic is much smaller. Contrails in this region are very seldom, so that each detected feature can be checked individually. We processed 42 passages of a NOAA 14 data set received at New Zealand. A total of 150,088 AVHRR lines were analyzed this way with our contrail detection algorithm. All features classified as contrail by the algorithm were verified by visual inspection. In case the observer was sure that the displayed feature was an artifact it was classified as a false detection. Only 0.008% of all pixels in the analyzed scenes around New Zealand are considered to be true contrails, while 0.097% seem to be artifacts. Most of the artifacts are cirrus streaks (90%), 2% are cloud borders, 7% are cloud streets, and 1% are of unidentified origin.

[25] To find out whether the false alarm rate varies across the scan line, FAR is plotted against the AVHRR element number. In Figure 5 we see that FAR is almost constant for the analyzed scan angles. It is sufficient to cut off the outer 100 pixels on both sides.

2.2.5. False alarm correction. [26] The rate of false alarms biases the rate of correct classifications. To reach an uninfluenced contrail frequency, FAR must be removed from the spatially averaged contrail coverage N'_{ct}. This correction is applied to the mean statistical results and thus is valid only for a large numbers of measurements. The FAR = 0.097% derived from the New Zealand data set is often much larger than the contrail coverage N'_{ct} derived in some parts of Europe. Obviously, FAR depends on the region considered. Some oceanic areas within the European data set, such

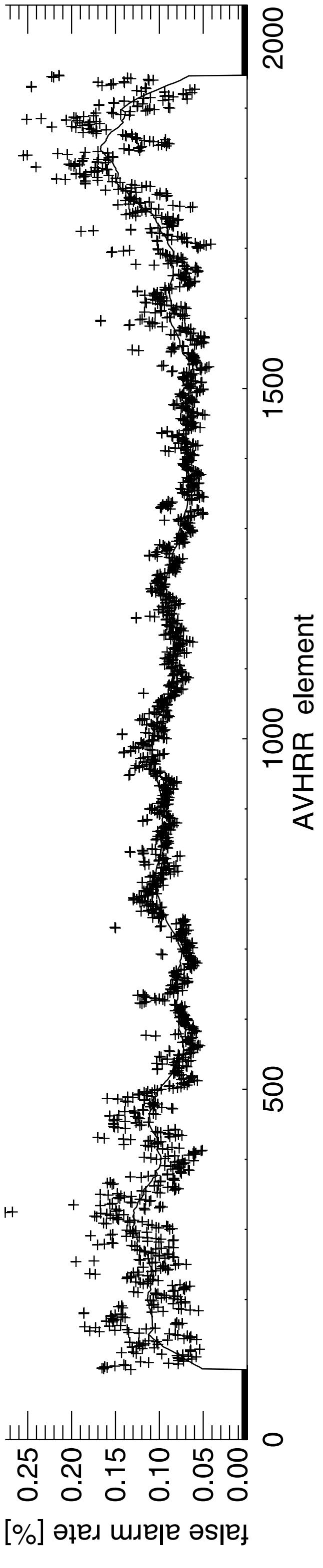

as the Atlantic north of Portugal, exhibit a rather large apparent contrail cover N'_{ct} of 0.1% in spite of low air traffic density. Some mountainous land regions, such as Croatia, exhibit a low cover N'_{ct} of 0.026%. Croatia belongs to the former Yugoslavia where air traffic was strongly restricted during the period March 1995 to February 1997. Therefore we interpret this cover as a consequence of false alarms.

[27] The variation of FAR appears to be related to the average standard deviation SDT_{12} of T_{12} for a 5 × 5 pixel kernel (see Figure 6). The algorithm normalizes the input images by SDT_{12} in order to allow operation of the algorithm with constant parameters throughout the year. The normalization step in the algorithm should also avoid misdetection of other linear structures like coastlines or mountain ridges. However, a connection between SDT_{12} and FAR remains. This is obvious from Figure 7 (left) where SDT_{12} averaged over 1° × 1° is plotted against N'_{ct} averaged over the same box size. The average value pair for the New Zealand (NZ) data set is included in Figure 7 (left). It fits very well to the European data. Together with the Croatia data (Cr), this finding is used to define the following linear regression:

$$\mathrm{FAR}\left(\overline{\mathrm{SDT}_{12}}\right) = 0.166 - 0.150\,\overline{\mathrm{SDT}_{12}} \geq 0. \qquad (4)$$

To avoid small-scale overshooting corrections, we smooth SDT_{12} by a Gauss-shaped filter (profile shown in Figure 4), producing $\overline{\mathrm{SDT}_{12}}$. In the following we calculate the false alarm corrected contrail frequency N''_{ct} by

$$N''_{ct} = N'_{ct} - \mathrm{FAR}\left(\overline{\mathrm{SDT}_{12}}\right), \qquad (5)$$

giving our best estimate for the contrail frequency independent from misdetections.

2.3. Detection Efficiency

[28] From the plot of the standard deviation $\overline{\mathrm{SDT}_{12}}$ against false alarm-corrected contrail frequency N''_{ct} one notices that normalization with SDT_{12} has also a strong influence on the amount of contrails detected. This fact was already recognized and corrected by *Mannstein et al.* [1999], but the correction has to be revised because of the newly established false alarm correction. As can be seen in Figure 7b, contrail frequency is much higher over regions that are quite homogeneous in the 12 μm channel. For example, over the ocean, SDT_{12} values are mostly around 0.5 K, and many contrails are detected in the same region. On the other hand, the number of detected contrails is sparse over thermally inhomogeneous areas.

[29] In regions with $\overline{\mathrm{SDT}_{12}}$ values above a threshold of 1.1 K the number of contrails detected is so small that it is impossible to derive statistically reliable results. Therefore we decided to eliminate regions from the analysis in which the annual average of $\overline{\mathrm{SDT}_{12}}$ exceeds this value. This criterion is fulfilled in particular over mountains such as the Alps and the Pyrenes.

[30] For the remaining regions the data are fitted by a linear regression, and this regression is used to correct for the effect of $\overline{\mathrm{SDT}_{12}}$ on N''_{ct}. This step clearly supposes that the relation between $\overline{\mathrm{SDT}_{12}}$ and N''_{ct} is constant throughout the analyzed region and that there is no accidental correlation of $\overline{\mathrm{SDT}_{12}}$ and air traffic intensity, for example, due to variable atmospheric conditions. Regional variations in the frequency of high-flying air traffic are likely responsible for the strong vertical spread in Figure 7. Correlating $\overline{\mathrm{SDT}_{12}}$ to air traffic fuel consumption according to *Schmitt and Brunner* [1997] results in a linear regression coefficient of 0.005, indicating that the

Figure 5. (opposite) FAR against AVHRR line element number revealing the scan angle. Analysis of 42 scenes for region New Zealand (NOAA 14 AVHRR data of April 1997).

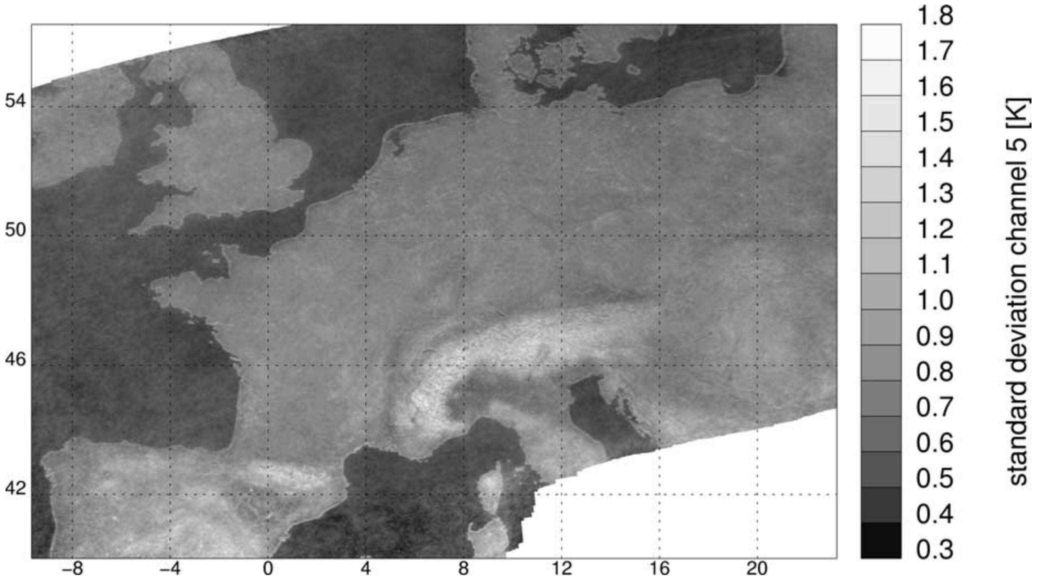

Figure 6. Average of the 5 × 5 pixel standard deviation SDT_{12} in temperature channel 5 from noon data in the period March 1995 to February 1997.

assumption of independence is valid. The resulting correlation between $\overline{\mathrm{SDT}_{12}}$ and N''_{ct} leads to a homogenized contrail coverage

$$N_{ct,\min} = \frac{1}{1 - 0.17/0.29\,\overline{\mathrm{SDT}_{12}}} N''_{ct}. \qquad (6)$$

In the following, (6) is used to correct the contrail coverage. Since the detection algorithm can only identify parts of all existing contrails and since we previously cut off false alarms, the homogenized contrail coverage $N_{ct,\min}$ represents a lower limit for the true area covered by line-shaped contrails. Because of the tuning of the algorithm to a low FAR, the detection efficiency DEF is far from being perfect. Comparing the homogenized contrail coverage to various other observations [*Rotter*, 1987; *Schumann and Wendling*, 1990; *Schumann and Reinhardt*, 1991; *Meyer*, 2000], the overall DEF was estimated to be 0.4 ± 0.2. By

$$N_{ct} = \frac{N_{ct,\min}}{\mathrm{DEF}} \qquad (7)$$

we finally get the resulting contrail coverage N_{ct} shown in Figure 8. This result includes all the mentioned corrections given by (5) and (6).

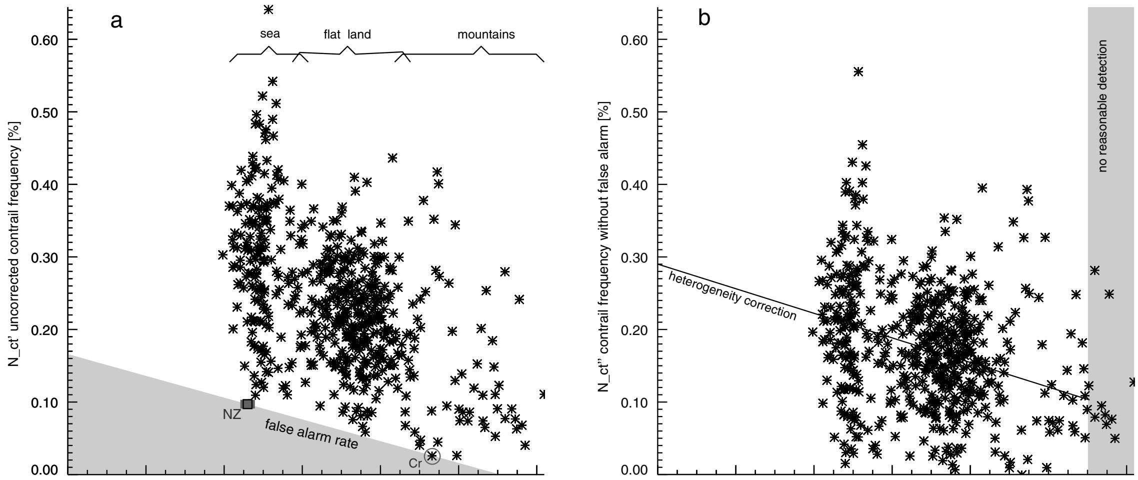

Figure 7. Average standard deviation $\overline{\mathrm{SDT}_{12}}$ over 1° × 1° boxes against (a) the uncorrected contrail frequency N'_{ct} and (b) the false alarm–corrected contrail frequency N''_{ct}. The points NZ and Cr in Figure 7a mean New Zealand data and Croatia, respectively.

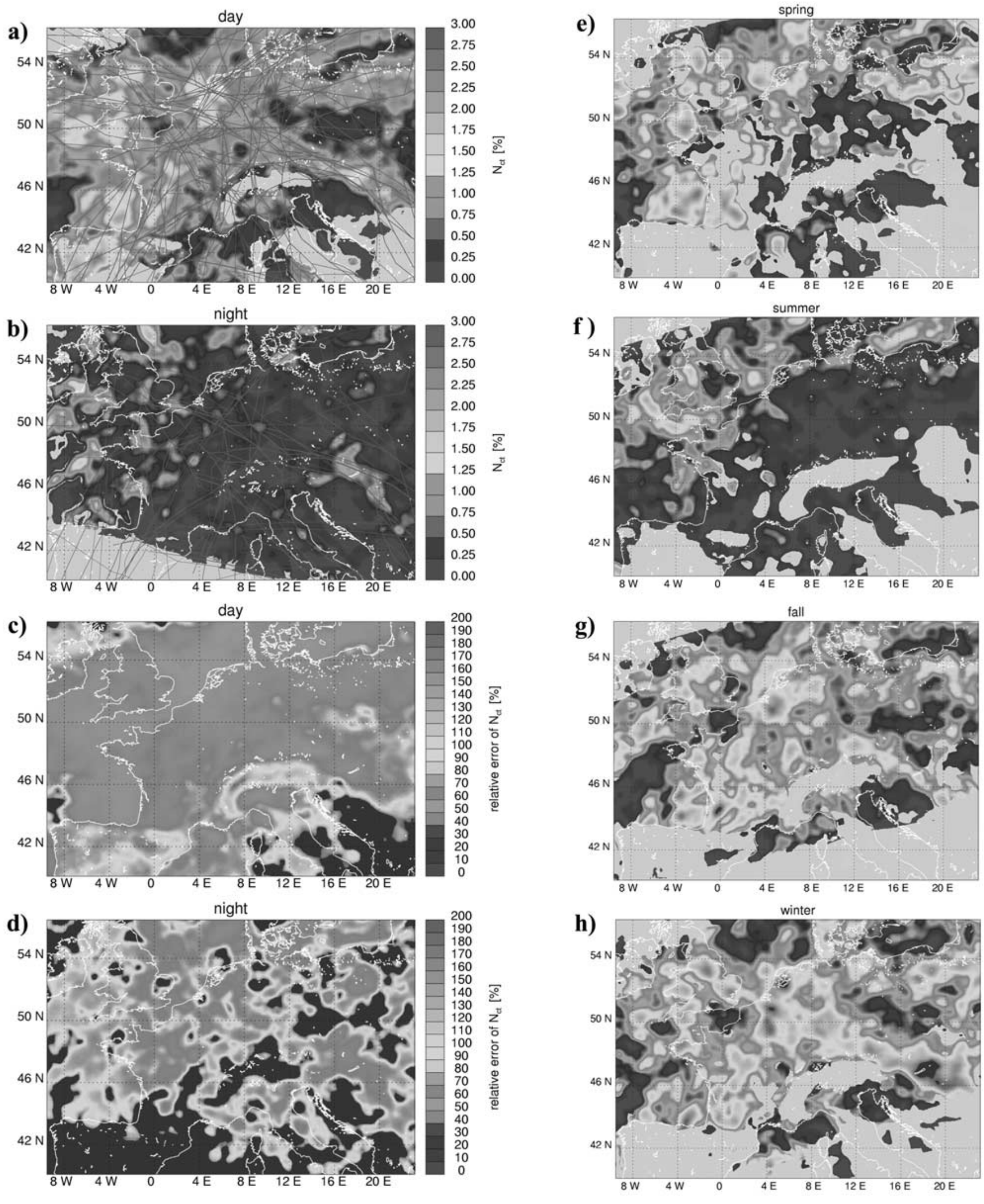

Figure 8. Mean coverage by line-shaped contrails. (a) The annual daytime coverage related to an average satellite overpass time of 1230 UTC. The overlay shows all actual flights in the contrail-relevant height interval from 8 to 14 km during the time slice 1000–1300 UTC on 2 days in 1996 (from flight plan data of EUROCONTROL). (b) The annual mean nighttime contrail coverage related to 0150 UTC (overlaid flights here related to the time interval from 2320 to 0220 UTC). The relative error of annual mean contrail coverage for (c) day and (d) night. The seasonal mean daytime coverage is shown: (e) spring, (f) summer, (g) fall, and (h) winter. Same color coding as for annual mean coverage (gray, areas not defined due to $\overline{\mathrm{SDT}_{12}} > 1.1$ K; beige, relative error > 100%). See color version of this figure at back of this issue.

An overlay of actual flight routes generated from flight activity data shows the plausibility of the shown contrail pattern.

[31] A precise determination of the detection efficiency is impossible because the truth (i.e., the true contrail coverage at the time of the satellite overpass) is not very well defined (how linear must the contrail be to get detected as such?) and no independent measurement of contrail coverage is available. To discriminate aged contrails from natural cirrus clouds would require identifying unique tracers (such as the composition of the ice particle residuals) or following the history of the cloud with high temporal and spatial resolution. The transition from a well-marked line-shaped contrail to a fuzzy cirrus cloud that might have been triggered by a contrail, using highly resolved time series, has been demonstrated in a case study with data from the geostationary satellite GOES by *Minnis et al.* [1998].

[32] Another source of ambiguity comes from the ambient cirrus clouds. Quite often, contrails form in regions where there is already a thin cirrus cloud. These contrails add no additional cloud coverage but alter the cloud optical and microphysical properties.

2.4. Resulting Contrail Coverage

[33] To derive statistically significant averages of contrail coverage, we processed 702 daytime and 232 nighttime scenes of NOAA 14 of the 2 year period starting in March 1995. For nighttime passes, only data of midseason months are available. The daytime contrail coverage (Figure 8a) is related to the typical NOAA 14 overpass time at 1230 UTC, while the nighttime contrail coverage is related to a typical overpass at 0150 UTC. Because of the daily shift of the nadir track of the NOAA polar orbiters, the overpass times can be 70 min earlier or later. The derived contrail cover (see Figure 8) shows a distribution with regional maxima up to 2.8% during day and 2% during night. At least for the daytime data the distribution fits very well to the air traffic pattern.

[34] The day/night ratio of observed contrail cover amounts to 2.9. This result matches well the day/night ratio of the total flight duration in the same region [*Schmitt and Brunner*, 1997]. Flight data obtained from the European Aviation Control Center (EUROCONTROL) show a day/night ratio of 3.7 within the contrail/relevant interval of 10–13 km altitude. The validity of our postprocessing scheme is supported by this result, in particular since the raw data would imply a much smaller value of $N'_{ct,\mathrm{noon}}/N'_{ct,\mathrm{night}} = 1.3$, while the not-homogenized values give $N''_{ct,\mathrm{noon}}/N''_{ct,\mathrm{night}} = 2.2$. This improvement was possible only by using a separate nighttime $\overline{\mathrm{SDT}_{12}}$ mask. The usage of different $\overline{\mathrm{SDT}_{12}}$ masks is strongly recommended because false alarms must be more frequent and detection efficiency higher over the more homogeneous background during nighttime than during daytime. FAR averaged over the whole displayed area is 0.10% during day and 0.07% during night. According to the regional differences of the $\overline{\mathrm{SDT}_{12}}$ masks the false alarm rate varies in the range of 0–0.15%. It is very low in regions with strong topography or a high probability of convective clouds. These are the areas where normalization of input data reduces the signal strongest in order to prevent misdetections.

[35] A constant DEF of 40% was used but the differing $\overline{\mathrm{SDT}_{12}}$ masks for night and day also have an impact on the homogenization step (see (6)), which leads to stronger enhancements of the daytime contrail distribution. As mentioned above, underlying clouds also have an influence on contrail detectability. Contrails are easy to recognize above more homogeneous stratiform clouds but harder to detect above convective clouds, which show features of smaller scale leading to higher $\overline{\mathrm{SDT}_{12}}$. Through the homogenization step these effects of underlying clouds are also taken into account in a statistical manner. For example, regions where stratiform clouds are frequent show less and thus get less enhanced by (6).

Table 1. Values of Mean Coverage by Line-Shaped Contrails N_{ct} for Night, Day, and Different Seasons Related to the Defined Areas Displayed in Figures 8a–8d

Time	Spring, %	Summer, %	Fall, %	Winter, %	Yearly, %
Night	0.28	0.11	0.41	0.21	0.25
Day	0.72	0.33	0.85	1.00	0.72
Mean	0.50	0.22	0.63	0.61	0.50

[36] The relative error of the derived contrail coverage is controlled by the available number of measurements n and the contrail coverage itself (see (3)). It also depends strongly on the ratio of FAR to N'_{ct}, in particular when N'_{ct} is only slightly larger than the average FAR. Combining all known errors according to the law of error propagation, the errors are calculated and mapped in Figure 8 for annual mean daytime and nighttime contrail coverage. The relative error can easily surpass 100% in areas in which the absolute amount of contrail cover is small. Therefore areas with relative errors exceeding both 100% relative error and 0.25% absolute error are marked as "undefined" in the contrail maps shown. In the other regions the relative error amounts typically to 50–100%.

[37] The region studied in this paper is a subset of the region that has been previously investigated by *Bakan et al.* [1994]. For daytime coverage, *Bakan et al.* [1994] derive an annual average of 0.88% in the region 40°–55°N and 10°W to 20°E, while our result for an estimated detection efficiency of DEF = 0.4 is 0.74%. This means that the daytime contrail coverage from *Bakan et al.* [1994] is ~20% higher than our result. For nighttime, *Bakan et al.* [1994] do not show maps of contrail coverage but state that it reaches 50% of the daytime values. From this we conclude that it must be about 0.44% while we get an average nighttime contrail coverage of 0.25%. Therefore nocturnal contrail coverage from *Bakan et al.* [1994] is about 75% higher than our value. The lower day/night ratio derived by the visual inspection appears reasonable since detection efficiency for human observers should also be higher above the more homogeneous nighttime background. Unfortunately, the human efficiency is difficult to quantify.

[38] As we estimate that the relative error of our data varies from 50 to 100%, the results of *Bakan et al.* [1994] are within the error margins. Nevertheless, we assume that visual interpretations tend to overestimate the contrail coverage. The human eye, in general, is "tricked" by rare events and tends to overestimate the area of narrow patterns. This effect may be reinforced by the fact that the AVHRR quicklooks analyzed by *Bakan et al.* [1994] were displayed on paper prints. Because of the granulation of the photographic paper, bright narrow features such as contrails can actually fill a wider area than contrails cover in reality.

[39] The annual cycle of contrail coverage is visualized in Figures 8a–8d. Mean values are listed in Table 1. During winter a relatively high contrail coverage of 1.0% prevails in most of the area. During fall the contrail pattern is similar with a slightly smaller average of 0.9%. The summer distribution resembles the contrail distribution during spring, but the mean coverage of 0.7% during spring is much higher than during summer when only 0.3% of the total area is covered by contrails. The low coverage during summer is mainly caused by very low contrail frequencies in the southern and eastern parts of the analyzed region.

3. Contrail Optical Depths

[40] The radiative forcing by contrails is mainly determined by the product of the area cover and the optical depth of contrails [*Meerkötter et al.*, 1999]. The contrail optical depth is the average optical depth of contrails without influence of the atmospheric background below or above the contrail layer. Obviously, the total

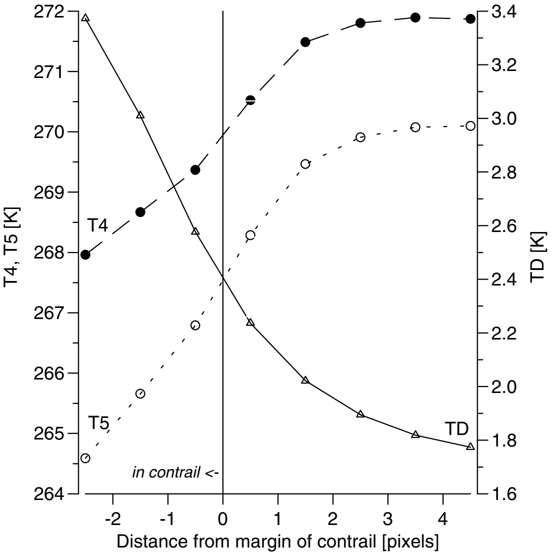

Figure 9. Mean brightness temperatures within contrail pixels and in their direct neighborhood. In the center of wide contrails the lowest temperatures are observed. Narrow contrails of one pixel width or margins of wider contrails are summarized at position −0.5. They often seem to consist of partially contrail-filled pixels. The plotted data represent the average for all contrails found in noon scenes.

optical depth of the atmosphere is higher than the pure contrail optical depth. Therefore methods that derive optical depths from single pixels without proper elimination of the background optical depth may be misleading.

[41] Further, the optical depth applied for calculation of contrail forcing should depend on the method used to derive contrail coverage. In this paper, area coverage is based on contrail detection from AVHRR data with its raw data pixel scale of ~1 km × 1 km. Many of the pixels classified as contrails are only partly filled by contrails, either because young contrails get detected that fill only a subset of the pixel area or because margins of wider contrails cross through the contrail pixel. In both cases those contrail pixels are partly filled, and their optical depth will be less than that of a pixel fully filled by a contrail of the same type. Therefore the needed contrail optical depth should be related to the same area classified as contrail. This kind of optical depth, which describes the average over the entire pixel for which the contrail coverage was derived, we call "effective optical depth".

[42] The effective contrail optical depth here is determined by a differential method that compares radiances of contrail pixels with those in their direct neighborhood. This is done by use of the radiances L_{11} in the infrared channel at 11 μm. For this purpose we calculate averages for shells with equal distance to the margin of contrails. Those shells are derived by successive application of the morphological operators "erode" and "dilate" [*Pratt*, 1991]. First, a margin of one pixel width is shaped from the original contrail mask by the erode operator. This results in the shells indicated by −1.5 in Figure 9. Further erosion leads to results only where contrail width is ≥5 pixels. As contrails of such a great width are not very frequent and our detection algorithm hardly can recognize these widespread fuzzy contrails, pixels of the −2.5 shell appear sparsely.

[43] Then we successively broaden the original contrail mask by use of the dilateoperator, which is the inverse to the erode operator. Thus shells are derived that are located outside the detected contrail pixel at positions numbered 0.5, 1.5,. . ., 4.5. For each of these shells the average radiance L_{11} is calculated. The mean radiances or brightness temperatures of each shell vary strongly because ambient temperatures in the contrail level T_{ct} and especially the background brightness temperature T_{11} are very variable. In order to obtain results characteristic for the mean over all background conditions it is essential to average over very many shells that cover all situations in which contrails appear throughout the year. The result for this is displayed in Figure 9.

[44] The blackbody radiances of 200–300 K warm bodies at 11 μm wavelength are approximately proportional to radiative fluxes. Therefore it easily can be seen that contrails reduce the outgoing broadband terrestrial flux F_{ter}. The flux depends mainly on the contrail infrared emissivity in question. Following *Platt and Stephens* [1980], the effective contrail emissivity for a wavelength of 11 μm is calculated by

$$\varepsilon_{e11ct}(\theta) = \frac{L_{11}(\theta) - L_{11ct}(\theta)}{L_{11}(\theta) - L_{B11}(T_{ct})}, \qquad (8)$$

where θ is the zenith angle, L_{11ct} is the average radiance of the contrail pixels, L_{11} is the average radiance of the surrounding pixels, and L_{B11} is the emitted radiance of a blackbody at temperature T_{ct} of the ambient temperature at the contrail level. The effective emissivity given in (8) includes absorption and scattering by contrail particles. However, to derive the optical depth from this emissivity, only the absorptive part ε_a is needed. According to *Platt and Stephens* [1980], for the scan angle interval of ±50° investigated here the absorptive emissivity ε_a is on average 13% smaller than ε_e. Because the horizontal extent of the observed contrails is usually much higher than their height, geometric length and thus emissivity is increasing with θ. Following *Platt and Stephens* [1980], we derive the vertical emissivity from

$$\varepsilon_{a11ct} = 1 - [1 - \varepsilon_{a11ct}(\theta)]^{\cos\theta} \qquad (9)$$

under the assumption of a flat Earth. Averaged over the analyzed scan angle interval, this procedure results in emissivities that are 19% smaller than the slant values. Finally, the absorptive vertical optical depth of contrails related to AVHRR channel 4 is obtained from

$$\delta_{a11ct} = -\ln(1 - \varepsilon_{a11ct}). \qquad (10)$$

[45] Unfortunately, this method may only be applied when the radiances get averaged over many contrails. The reason is the strong variability of the background radiances especially over land. Accidentally, it may happen that a contrail lines up over a relatively warm surface while the surrounding surface is a little colder. These situations that would lead to irrational negative emissivities get avoided when averaging over very many pixels. From our channel 4 data of the full analysis period (February 1995 to March 1997) we get an annual average of L_{11ct} = 5.763 W m^{-2} μm^{-1} sr^{-1} for contrail pixels. This value is computed by taking the arithmetic average of pixels in the three contrail shells (−2.5, −1.5, and −0.5). The proper background value should be free of influences from the contrail considered. Therefore we use only pixels far enough apart from the contrail. As can be seen in Figure 9, this is the case when utilizing pixels at positions 3.5 and 4.5. This results in L_{11} = 6.050 W m^{-2} μm^{-1} sr^{-1}.

[46] Because of the low emissivity of contrails, it was not possible to derive contrail temperature directly. For the same reason it is not feasible to get sound contrail top heights from AVHRR. Therefore we assume a contrail height of 10 km, which is the height with the most flight activities over Europe, and use an estimated

contrail temperature of T_{ct} = 224.7 K, which is the annual mean temperature in the summer and winter midlatitude standard atmospheres at this altitude. This leads to $L_{B11} = 2.199$ W m^{-2} μm^{-1} sr^{-1}. From this $\varepsilon_{a11ct} = 0.051$ or $\delta_{a11ct} = 0.053$ is derived.

[47] The vertical optical depth δ_{a11ct} for the 11 μm channel is used to determine the broadband visible optical depth centered at a wavelength of 0.55 μm. For this purpose we assume a particle size distribution for contrails as measured by *Strauss et al.* [1997]. This distribution is characterized by an effective diameter D_e of 34 μm and is representative for contrails with an age of about half an hour. Assuming spherical contrail particles, a conversion factor of 2.1 is derived from Mie theory. This results in $\delta_{\mathrm{vis}} = 0.11$ for a wavelength of 0.55 μm.

[48] The error in the effective optical depth of contrails δ_{vis} derived this way may be estimated by the sensitivity of the result to various input parameters. A parameter causing a large uncertainty is the average temperature at the contrail level. If T_{ct} is modified by +10 K (−10 K), the optical depth changes by +19% (−14%). Another source of uncertainty is the infrared to visible conversion factor, which depends on the particle size spectrum and particle shapes. Assuming a smaller effective diameter D_e, the conversion factor can be much higher, which leads to strong underestimation of visible optical depth. According to Mie theory the conversion factor for a 30 min old contrail with $D_e = 10-11$ μm (case U in *Schröder et al.* [2000]) would be 2.8, implying an increase of δ_{vis} by +33%. If a particle size of D_e = 5.4 μm as measured for a 10 min old contrail [*Schröder et al.*, 2000] would be more representative for contrail particle sizes, the visible optical depth would be twice as large. However, other studies report much larger effective contrail particle diameters, in the range from 10 to 40 μm [*Duda et al.*, 1996, 1998]. Hence the assumed contrail particle size of 34 μm according to *Strauss et al.* [1997] seems to represent quite well the contrails of typically half an hour age. This age seems to be typical for most of the observed contrails in the satellite data. Therefore an error of −15% to +80% is estimated, yielding a visible optical depth in the range of 0.1–0.2.

[49] The value of the optical depth of contrails found here falls into the lower range of values reported so far. Former estimates have been derived from case studies based on a few measurements. Such case studies tend to select the more pronounced contrails. Ground-based Lidar measurements at Garmisch, southern Germany, imply a contrail slant optical depth of about 0.2 [*Jäger et al.*, 1998; *Freudenthaler*, 2000]. It appears plausible that the partially contrail-filled pixels exhibit a smaller mean optical depth than the maximum values reported from individual measurements.

[50] Very recently, *Ponater et al.* [2002] computed the contrail optical depth from a contrail model within a global circulation model. The model results vary strongly spatially with the temperature- and pressure-dependent amount of water available for ice formation, and the mean visible optical depth computed in this model over Europe amounts to about 0.06. Hence the computed value is even smaller than the value that we derived from the satellite data. The differences may be caused by various model assumptions, as discussed by *Ponater et al.* [2002].

4. Radiative Forcing

[51] Finally, we estimate the radiative forcing caused by the contrails at TOA. The radiative forcing usually decreases from TOA to the ground and may be negative at the ground even for positive values at TOA [see *Meerkötter et al.*, 1999]. For contrails in the upper troposphere the differences between TOA and top of troposphere radiative forcing values have been estimated to amount to about 10% [*Meerkötter et al.*, 1999]. For distances much greater than contrail width, *Schulz* [1998] showed that three-dimensional (3-D) influences will be negligible for radiative fluxes. Therefore 1-D radiative transfer calculations are applicable. *Meerkötter et al.* [1999] compared various 1-D codes and found that they all agree well within a maximum difference of 7% for contrail net radiative forcing. Therefore we use one of the tested codes, the Matrix Operator Model (MOM).

Table 2. TOA Net Radiative Forcing Coefficients, i.e., Forcing for 100% Contrail Coverage[a]

Time	Summer		Winter	
	$\Delta F_{\mathrm{ocean}}$, W m^{-2}	ΔF_{land}, W m^{-2}	$\Delta F_{\mathrm{ocean}}$, W m^{-2}	ΔF_{land}, W m^{-2}
Night	13.5	13.1	12.3	11.5
Day	5.7	7.7	−6.8	4.1
Mean	8.9	9.9	4.4	8.4

[a] Daytime values are related to the daily average between sunrise and sunset at a latitude of 50°N, nighttime vice-versa. Optical depth $\delta_{\mathrm{vis}} = 0.11$, and surface albedo over land is 0.2 and over oceans is 0.05. Spherical ice particles and size distribution are according to *Strauss et al.* [1997].

[52] The radiative transfer calculations are performed for contrails with the satellite-derived optical thickness δ_{vis} of 0.11. Land and ocean regions are treated separately using an albedo of 5% for water surfaces and 20% land surfaces. Further, we assume spherical ice particles with a size distribution as measured by *Strauss et al.* [1997]. Local cloud cover below the contrails is not included in these calculations. The corresponding radiative forcing coefficients, i.e., the forcing per unit cover for completely contrail-covered pixels, are listed in Table 2. Obviously, a contrail cover heats most during night but also heats relatively strongly for high Sun altitude angles (midday in summer) [*Meerkötter et al.*, 1999]. For low Sun altitude and low surface albedo, for example, over sea, a moderate cooling is expected even at TOA.

[53] The radiative forcing is the product of the coefficients shown in Table 2 with the actual contrail coverage. Because of the lack of more temporal sampling points, we have to take the contrail coverage derived for noon as the representative distribution for daytime and the distribution derived from NOAA 14 night passages as the representative distribution for nighttime. As there were only 8 months of night data available, we could only separate two seasons: summer from March to August and winter from September to February. Otherwise, the coverage results would not be significant. The forcing coefficients further are weighted by the relative average day length according to latitude and season. The resulting contrail forcing maps are displayed in Figure 10.

[54] The patterns of the radiative forcing are similar to that of the contrail coverage shown in Figure 8. We clearly see that the relatively small coverage during night leads to an efficient forcing that is of about the same magnitude as that during daytime in summer and even larger than during daytime in winter (see Table 3). Distinguishing shortwave and longwave fluxes for daytime (see Table 4), one recognizes that absolute values of the separate forcing terms are high during the day, but they get counterbalanced because of their opposite direction.

[55] The scheme used to estimate the contrail radiative forcing is very simple and contains several approximations that may be sources of errors. Systematic errors are to be expected, for example, from disregarding cloud cover below or above the contrails. Clouds in most cases increase the albedo compared to the cloud-free case. Therefore the cooling effect of contrails introduced by enhanced albedo in the shortwave spectrum is much smaller over such clouds. On the other hand, the longwave radiative forcing would be reduced for contrails over cold clouds. *Meerkötter et al.* [1999] give an example where an optically thick low-level water cloud at 2–3 km altitude is added below a contrail of optical depth 0.52 in a midlatitude summer standard atmosphere with surface albedo of 0.2. This enhances the net radiative forcing by the contrail by 8%. The average frequency of low clouds in the area analyzed here is around 40% [*Rossow et al.*, 1996]. For

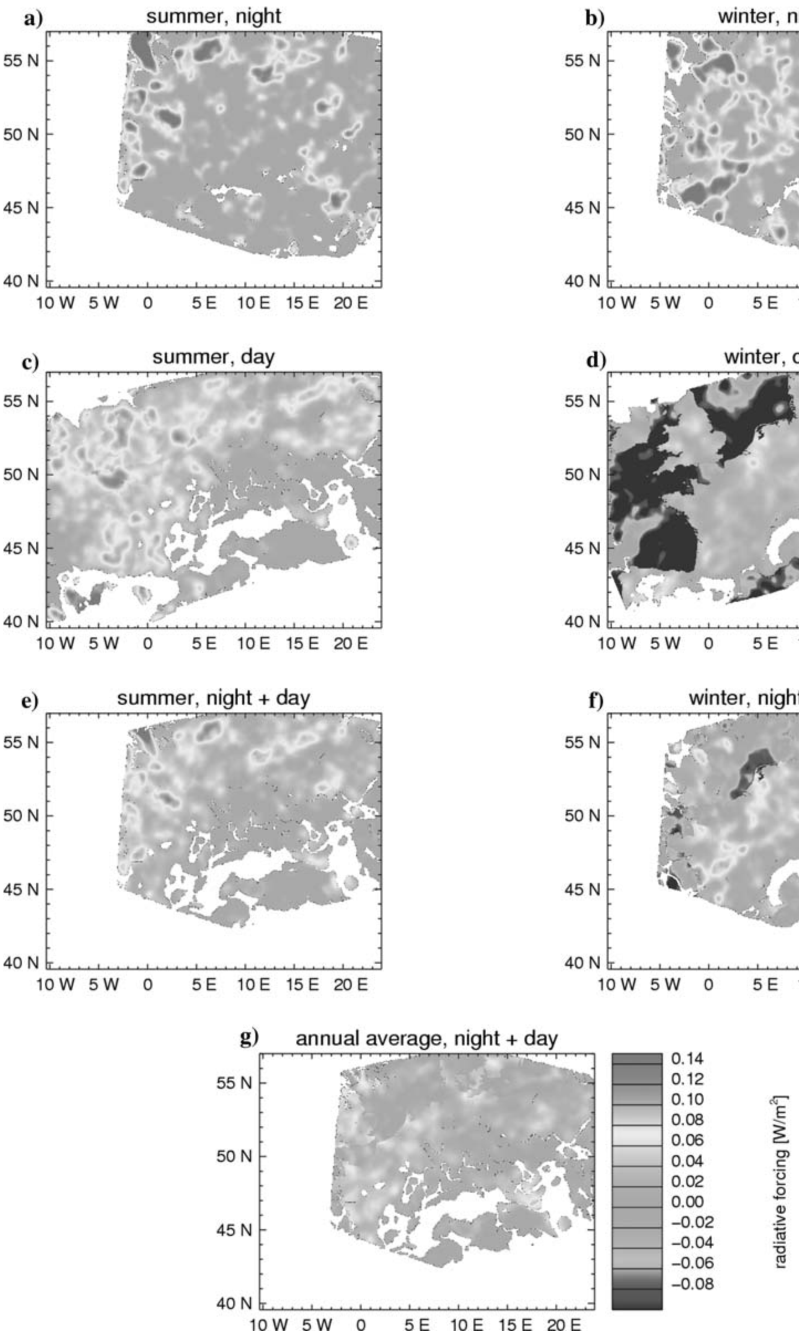

Figure 10. Contrail radiative forcing related to TOA: (a) summer and (b) winter nighttime average, (c) summer and (d) winter daytime average, (e) summer and (f) winter full day average and (g) the synthesis of all, the annual mean contrail forcing. In some maps, for example, Figure 10a, some values exceed the color table. See Table 3 for maxima. (Areas with relative errors of contrail coverage above 100% are blanked). See color version of this figure at back of this issue.

Table 3. Net Radiative Forcing at TOA Based on Satellite Observations of Coverage Through Line-Shaped Contrails and Effective Mean Optical Depth Separated for Night, Day, and Daily Average[a]

	Summer $\overline{\Delta F}$, W m^{-2}			Winter $\overline{\Delta F}$, W m^{-2}		
	Minimum	Mean	Maximum	Minimum	Mean	Maximum
Night	0.000	0.031	0.439	0.000	0.040	0.259
Day	0.000	0.035	0.129	−0.420	−0.002	0.089
Daily average	0.000	0.033	0.225	−0.147	0.018	0.135

[a] The given values are all related to the same area, which is the region with valid data in Figure 10g.

random overlap this leads to an approximate underestimate of contrail forcing in the range of 5–25%.

[56] A further origin of unceratinty is introduced by the uncertainty in the optical depth. For small optical depth values below 0.5 the error range of −15% to +80% estimated for the contrail optical depth implies an error of the same size in the radiative forcing. An underestimate may also arise from the available sampling times, which cluster near 1230 and 0150 UTC. It is an advantage that the actual NOAA overpass times of the selected scenes vary ±70 min from day to day, which makes the distributions slightly more representative. From air traffic data (0600–2000, however, we known that flight intensity over Europe is almost constant during daytime UTC) and has its minimum in the second half of the night (0100–0300 UTC). Therefore the derived daytime cover should be quite representative, but nighttime coverage will be underestimated by about 40% as the evening traffic is not probed. Because contrails during nighttime are very important for the radiation budget, this underestimation of contrail coverage through missing sampling points in the morning and evening hours can increase the given daily net radiative forcing for about 50%.

[57] A missing adaptation of $\overline{\mathrm{SDT}_{12}}$ to seasonal values leads through (4) to a 10% daytime (3% nighttime) underestimate of contrail coverage during summer and an overestimate of about 3% for daytime (1% for nighttime) during winter. Because contrails show a stronger forcing during summer, the overall effect of this error may increase forcing by 1–4%. Another error resulting from the missing adaptation of surface temperatures to actual values is estimated to cause errors in the forcing of about −10% to +20% [*Meerkötter et al.*, 1999]. The assumption of spherical particles may result in less backscatter of solar radiation and hence tends to overestimate the net forcing by possibly 20% [*Meerkötter et al.*, 1999].

[58] Thus the actual net contrail forcing may deviate considerably from that given in Figure 10 and Table 3. An annual average net radiative forcing of 0.03 W m^{-2} is derived as the best estimate from the analysis for the west European region under consideration. From the knowledge we have today, however, it could also reach down near to zero and up to 0.08 W m^{-2}. For comparison, the radiative forcing value estimated by *Minnis et al.* [1999] for the same west European region amounts to 0.4 W m^{-2}, which is 1 order of magnitude larger than our best estimate.

5. Conclusions and Outlook

[59] The cover, optical depth, and radiative forcing due to contrails over Europe have been derived from 2 years of satellite observations. The influences of false detections and varying detection efficiency on the amount of contrail cover depends mainly on the thermal homogeneity of the background and may be partially corrected as a function of the standard deviation of brightness temperature variations. The mean contrail cover distribution is typically determined with an error of order 50–100%.

[60] A first estimate of the mean effective optical depth of contrails on average over the west European region is 0.11 in the visible range. The value might be higher (up to 0.2) if contrails are composed of smaller particles than assumed. This result is smaller than values reported from case studies in the past because many of the detected contrails fill the ~1 km wide AVHRR pixels only partly. This effective optical depth is more suited for radiative forcing calculations than local maximum values because the effective value provides the correct product of contrail coverage and optical depth on average over the satellite pixels. Contrary to former measurements, we corrected optical depth for viewing angle effects which decrease δ for a further 19%. Different from case studies, our value represents a long-term average.

[61] The annual mean contrail radiative forcing value derived for the achieved contrail cover and optical depth values is about 0.03 W m^{-2}. This value is about 2 order of magnitude smaller than the result of *Minnis et al.* [1999] for the region analyzed here. The large differences can be understood by the fact that *Minnis et al.* [1999] assumed a 3 times higher contrail optical depth (in the absence of better data) and used a 70% larger contrail coverage than found here on the basis of the analysis of *Sausen et al.* [1998]. The difference in coverage is still within the uncertainty range of our data, but contrail optical depth values seem to be clearly smaller on average than was assumed earlier, at least for the European region analyzed in this study. In this paper the radiative forcing of contrails was only calculated for clear-sky cases, even though many contrails get detected over mostly stratiform clouds. Depending mainly on the cloud top height of the underlying cloud cover, the net radiative forcing may be up to 25% higher.

[62] The finding of a relatively small radiative forcing by contrails should not be generalized without further investigations. The present study determined a regional contrail coverage smaller than was assumed in the past, but this cannot easily be extrapolated to the global scale. Preliminary results for other regions (southeast Asia and northern America) presented by *Mannstein et al.* [2000] tend to show higher contrail coverage values in relation to those computed by *Ponater et al.* [2002] or *Sausen et al.* [1998]. We recommend further observations of contrails preferably in regions where air traffic is strong enough to produce a noticeable amount of contrails. Strongly needed is a study that compares all contrail observations achieved until now with global simulations.

[63] The study of *Ponater et al.* [2002] indicates that the optical depth of contrails may be larger in the main traffic regions over North America than over Europe. Further studies on contrails should try to focus on their optical depth. We assume that the applied contrail detection algorithm works also with Moderate-Resolution Imaging Spectroradiometer (MODIS) data. This instrument may give a more detailed view on contrail bulk properties.

[64] Additional information on contrail height will be a benefit to give more realistic estimates of radiative forcing. Our contrail detection algorithm was successfully applied to data of Along

Table 4. Here We Separate the Values Given in Table 3 for the Radiative Forcing During Daytime Into the Shortwave and Longwave Portions

	Forcing, $\overline{F}$, W m^{-2}		
	Minimum	Mean	Maximum
	Summer Day		
Shortwave	−0.119	−0.026	0.000
Longwave	0.000	0.061	0.245
	Winter Day		
Shortwave	−0.746	0.111	0.000
Longwave	0.000	0.108	0.344

Track Scanning Radiometer (ATSR2) onboard the ERS-2 satellite, which enables derivation of contrail heights from its stereo view.

[65] The daily cycle of air traffic and contrail formation also needs observational proof. The high temporal resolution of geostationary satellites would help to answer this question. Unfortunately, we see only little chances to detect automatically contrails in these data because geometrical resolution will not be sufficient even for Meteosat Second Generation (MSG).

[66] Air traffic is still growing rapidly. We recommend investigating long-term AVHRR time series to check for an increase in contrail coverage.

[67] One should also keep in mind that air traffic may influence climate not only by contrails but also, for example, by emitting or inducing radiatively active gases and particles [*IPCC*, 1999]. This paper accounts only for line-shaped contrails that can be recognized by our pattern recognition algorithm. The climatic impact of cirrus clouds that evolved from contrails or cirrus that might be caused by air traffic-enhanced aerosols is still to be determined.

[68] **Acknowledgments.** This study has been partially supported by the German Federal Ministry for Education and Research (BMBF) within the DLR-BMBF project Schadstoffe in der Luftfahrt and the European Commission's research program on Environment and Climate within the CLOUDMAP project (contact ENV4 CT97-0399). We thank H. Larsen from the National Institute of Water and Atmospheric Research for AVHRR data received in New Zealand and EUROCONTROL for data on planned flight activity over Europe. A preliminary version of this paper was discussed at the European workshop on Aviation, Aerosols, Contrails and Cirrus Clouds (A2C3) in Seeheim, Germany, 10–12 July 2000.

References

Bakan, S., M. Betancor-Gothe, V. Gayler, and H. Grassl, Contrail frequency over Europe from NOAA-satellite images, *Ann. Geophys.*, *12*, 962–968, 1994.

Betancor-Gothe, M., M. Dreyer, S. Bakan, and C. Constanzo, Ground based passive remote sensing of ice clouds with scattered solar radiation in the near infrared, *Phys. Chem. Earth, Part B*, *24*, 219–224, 1999.

Boucher, O., Air traffic may increase cirrus cloudiness, *Nature*, *397*, 30–311, 1999.

Duda, D. P., J. D. Spinhirne, and W. Hart, Split-window retrieval of particle size and optical depth in contrails located above horizontally inhomogeneous ice clouds, *Geophys. Res. Lett.*, *23*, 3711–3714, 1996.

Duda, D. P., J. D. Spinhirne, and W. Hart, Retrieval of contrail microphysical properties during sucess by the split-window method, *Geophys. Res. Lett.*, *25*, 1149–1152, 1998.

Duda, D. P., P. Minnis, and L. Nguyen, Estimates of cloud radiative forcing in contrail clusters using GOES imagery, *J. Geophys. Res.*, *106*, 4927–4937, 2001.

Fahey, D. W., and U. Schumann, Aviation produced aerosols and cloudiness, in *Aviation and the Global Atmosphere*, edited by J. E. Penner, et al., *IPCC Spec. Rep.*, pp. 65–120, Cambridge Univ. Press, New York, 1999.

Fortuin, J., R. van Dorland, W. M. F. Wauben, and H. Kelder, Greenhouse effects of aircraft emissions as calculated by a radiative transfer model, *Ann. Geophys.*, *13*, 413–418, 1995.

Freudenthaler, V., Lidarmessungen der räumlichen Ausbreitung sowie mikrophysikalischer und optischer Parameter von Flugzeugkondensstreifen, Ph.D. thesis, Univ. Hohenheim, Garmisch, Germany, 2000.

Gardner, R. M., et al., The ANCAT/EC global inventory of NO_x emissions from aircraft, *Atmos. Environ.*, *31*, 1751–1766, 1997.

Gayet, J.-F., G. Febvre, G. Brogniez, H. Chepfer, W. Renger, and P. Wendling, Microphysical and optical properties of cirrus and contrails: Cloud field study on 13 October 1989, *J. Atmos. Sci.*, *53*, 126–138, 1996.

Gierens, K., R. Sausen, and U. Schumann, A diagnostic study of the global coverage by contrails, part II, Future air traffic scenarios, *Theor. Appl. Clim.*, *63*, 1–9, 1999.

Henderson, S. C., and U. K. Wickrama, Aircraft emissions: Current inventories and future scenarios, in *Aviation and the Global Atmosphere*, edited by J. E. Penner et al., *IPCC Spec. Rep.*, pp. 291–332, Cambridge Univ. Press, New York, 1999.

International Panel on Climate Change (IPCC), *Climate Change 1995: The Science of Climate Change*, edited by J. T. Houghton, et al., Cambridge Univ. Press, New York, 1996.

International Panel on Climate Change (IPCC), *Aviation and the Global Atmosphere*, edited by J. E. Penner, et al., 370 pp., Cambridge Univ. Press, New York, 1999.

Jäger, H., V. Freudenthaler, and F. Homburg, Remote sensing of optical depth of aerosols and clouds related to air traffic, *Atmos. Environ.*, *32*, 3123–3127, 1998.

Kästner, M., K. T. Kriebel, R. Meerkötter, W. Renger, G. Ruppersberg, and P. Wendling, Comparison of cirrus height and optical depth derived from satellite and aircraft measurements, *Mon. Weather Rev.*, *121*, 2708–2717, 1993.

Liou, K. N., Influence of cirrus clouds on weather and climate processes: A global perspective, *Mon. Weather Rev.*, *114*, 1167–1198, 1986.

Mannstein, H., R. Meyer, and P. Wendling, Operational detection of contrails from NOAA-AVHRR-data, *Int. J. Remote Sens.*, *20*, 1641–1660, 1999.

Mannstein, H., C. Leiter, R. Meyer, P. Wendling, P. Minnis, and R. Palikonda, Regional contrail coverage data estimated from AVHHR-data, paper presented at Meteorological Satellite Data User's Conference, Eur. Org. for the Exploit of Meteorol. Satell., Bologna, Italy, 2000.

Meerkötter, R., U. Schumann, D. R. Doelling, P. Minnis, T. Nakajima, and Y. Tsushima, Radiative forcing by contrails, *Ann. Geophys.*, *17*, 1080–1094, 1999.

Meyer, R., Regionale Kondensstreifen-Bedeckung aus Satellitendaten und ihr Einfluss auf den Strahlungshaushalt, *DLR-Forschungsbericht 2000-26*, Dtsch. Zentrum für Luft- und Raumfahrt, Cologne, Germany, 2000.

Minnis, P., D. F. Young, D. P. Garber, L. N. Nguyen, W. L. Smith Jr. and R. Palikonda, Transformation of contrails into cirrus during SUCCESS, *Geophys. Res. Lett.*, *25*, 1157–1160, 1998.

Minnis, P., U. Schumann, D. R. Doelling, K. M. Gierens, and D. W. Fahey, Global distribution of contrail radiative forcing, *Geophys. Res. Lett.*, *26*, 1853–1856, 1999.

Palikonda, R., P. Minnis, L. Nguyen, D. P. Garber, W. L. Smith Jr., and D. F. Young, Remote sensing of contrails and aircraft altered cirrus clouds, in *Impact of Aircraft Emissions Upon the Atmosphere, Paris, 15th–18th October*, Off. Natl. d'Etudes et de Rech. Aérospatiales, Chantillon, Paris, 1996.

Platt, C. M. R., and G. L. Stephens, The interpretation of remotely sensed high cloud emittances, *J. Atmos. Sci.*, *37*, 2314–2322, 1980.

Ponater, M., S. Marquart, and R. Sausen, Contrails in a comprehensive global climate model: Parameterization and radiative forcing results, *J. Geophys. Res.*, 10.1029/2001JD000429, 2002.

Pratt, W. K., *Digital Image Processing*, 2nd ed., John Wiley, New York, 1991.

Rossow, W., A. Walkewr, D. Beuschel, M. Roiter, *International Satellite Cloud Climatology Project (ISCCP)—Documentation of New Cloud Datasets*, Goddard Inst. for Space Stud., New York, 1996. (Available at http://isccp.giss.nasa.gov.)

Rotter, M., Auswirkungen von Flugzeugkondensstreifen auf die Sonnenbeobachtung und die Bewölkungsverhältnisse in Kärnten, Ph.D. thesis, Univ. Graz, Graz, Austria, 1987.

Sausen, R., K. Gierens, M. Ponater, and U. Schumann, A diagnostic study of the global coverage by contrails, part I, Present day climate, *Theor. Appl. Clim.*, *61*, 127–141, 1998.

Schmitt, A., and B. Brunner, Emissions from aviation and their developement over time, in *Pollutants From Air Traffic—Results of Atmospheric Research 1992–1997*, edited by A. Schumann et al., *DLR-Forschungsber. 97–04*, pp. 37–52, Dtsch. Zentrum für Luft- und Raumfahrt, Cologne, Germany, 1997.

Schröder, F., B. Kärcher, C. Duroure, J. Ström, A. Petzold, J.-F. Gayet, B. Strauss, and P. Wendling, On the transition of contrails into cirrus clouds, *J. Atmos. Sci.*, *57*, 464–480, 2000.

Schulz, J., On the effect of cloud inhomogeneity on area averaged radiative properties of contrails, *Geophys. Res. Lett.*, *25*, 1427–1430, 1998.

Schumann, U., On conditions for contrail formation from aircraft exhausts, *Meteorol. Z.*, *5*, 4–23, 1996.

Schumann, U., Influence of propulsion efficiency on contrail formation, *Aerosp. Sci. Technol.*, *4*, 391–401, 2000.

Schumann, U., Contrail cirrus, in *Cirrus*, edited by D. Lynch, pp. 231–255, Oxford Univ. Press, New York, 2001.

Schumann, U., and M. E. Reinhardt, Studies on the effect of high-flying air traffic on the atmosphere, paper presented at *42nd Congress of the International Astronautical Federation Montreal, Que., Canada,* 1991.

Schumann, U., and P. Wendling, Determination of contrails from satellite data and observational results, in *Lecture Notes in Engineering: Air Traffic and the Environment—Background, Tendencies and Potential*, edited by U. Schumann, vol. 60, pp. 140–153, Springer-Verlag, New York, 1990.

Schumann, U., R. Busen, and M. Plohr, Experimental test of the influence of propulsion efficiency on contrail formation, *J. Aircr.*, *37*, 1083–1087, 2000.

Spinhirne, J. D., W. Hart, and D. P. Duda, Evolution of the morphology and microphysics of contrail cirrus from airborne remote sensing, *Geophys. Res. Lett.*, *25*, 1153–1156, 1998.

Strauss, B., R. Meerkötter, B. Wissinger, P. Wendling, and M. Hess, On the regional climatic impact of contrails—Microphysical and radiative properties of contrails and natural cirrus clouds, *Ann. Geophys.*, *15*, 1457–1467, 1997.

Sussmann, R., Vertical dispersion of an aircraft wake: Aerosol-lidar analysis of entrainment and detainment in the vortex regime, *J. Geophys. Res.*, *104*, 2117–2129, 1999.

H. Mannstein, R. Meerkötter, R. Meyer, U. Schumann, and P. Wendling, Institut für Physik der Atmosphäre, Deutsches Zentrum für Luft- und Raumfahrt (DLR), DLR Oberpfaffenhofen, 82234, We, Germany. (Hermann.Mannstein@dlr.de; Ralf.Meerkoetter@dlr.de; Richard.Meyer@dlr.de; Ulrich.Schumann@dlr.de; Peter.Wendling@dlr.de)